

Article

Fabrication and Characterization of Hydrophobic Cellulose Nanofibrils/Silica Nanocomposites with Hexadecyltrimethoxysilane

Gi-Hong Kim ¹, Dong-Ho Kang ¹, Bich-Nam Jung ^{1,2} and Jin-Kie Shim ^{1,*}

¹ Korea Packaging Center, Korea Institute of Industrial Technology, Bucheon 14449, Korea; kakamate@kitech.re.kr (G.-H.K.); kangppp@kitech.re.kr (D.-H.K.); jbn5666@kitech.re.kr (B.-N.J.)

² Department of Chemical and Biological Engineering, Korea University, Seoul 02841, Korea

* Correspondence: jkshim@kitech.re.kr; Tel.: +82-32-650-4771

Abstract: Cellulose nanofibrils (CNFs) have attracted much attention because of their renewability and potential biocompatibility. However, CNFs are extremely hydrophilic due to the presence of a large number of hydroxyl groups, limiting their use as a water-resistant material. In this work, we controlled the adsorption behavior of silica nanoparticles on the surface of CNFs by adjusting the synthesis conditions. The silica nanoparticle size and packing efficiency on the CNF surface could be controlled by varying the ammonium hydroxide and water concentrations. In addition, hexadecyltrimethoxysilane (HDTMS) was successfully grafted onto CNF or CNF/silica nanocomposite surfaces, and the quantitative content of organic/inorganic substances in HDTMS was analyzed through XPS and TGA. The HDTMS-modified CNF/silica nanocomposites were more advantageous in terms of hydrophobicity than the HDTMS-modified CNF composites. This is because the silica nanoparticles were adsorbed on the surface of the CNFs, increasing the surface roughness and simultaneously increasing the amount of HDTMS. As a result, the HDTMS-modified CNFs showed a water contact angle (WCA) of $\sim 80^\circ$, whereas HDTMS-modified CNF/silica nanocomposites obtained superhydrophobicity, with a WCA of up to $\sim 159^\circ$. This study can provide a reference for the expansion of recyclable eco-friendly coating materials via the adsorption of silica nanoparticles and hydrophobic modification of CNF materials.

Keywords: cellulose nanofibrils; CNF/silica nanocomposites; hexadecyltrimethoxysilane; superhydrophobicity



Citation: Kim, G.-H.; Kang, D.-H.; Jung, B.-N.; Shim, J.-K. Fabrication and Characterization of Hydrophobic Cellulose Nanofibrils/Silica Nanocomposites with Hexadecyltrimethoxysilane. *Polymers* **2022**, *14*, 833. <https://doi.org/10.3390/polym14040833>

Academic Editor: Agnieszka Tercjak

Received: 21 January 2022

Accepted: 17 February 2022

Published: 21 February 2022

Publisher's Note: MDPI stays neutral with regard to jurisdictional claims in published maps and institutional affiliations.



Copyright: © 2022 by the authors. Licensee MDPI, Basel, Switzerland. This article is an open access article distributed under the terms and conditions of the Creative Commons Attribution (CC BY) license (<https://creativecommons.org/licenses/by/4.0/>).

1. Introduction

Environmental issues due to plastics are increasing the demand to replace petroleum-based materials with eco-friendly natural materials. Cellulose, the most abundant resource on earth, has gained substantial attention owing to its renewability, recyclability, biodegradability, nontoxicity, light weight, and good mechanical properties [1–5]. The various types of nanocellulose can be classified according to their width and length; these include cellulose nanocrystals (CNCs), cellulose nanofibrils (CNFs), and cellulose microfibrils (CMFs) [3,6]. CNCs have a short, rod-like shape around 2–20 nm in width and around 100–500 nm in length [7]. CNFs have a long, fibrillar shape around 1–100 nm in width and around 500–2000 nm in length [8,9]. The applications of nanocellulose are limited due to its lack of hydrophobicity, which is caused by the presence of a large number of hydroxyl groups (–OH). Low moisture resistance is one of the most important factors to consider in practical applications, as it seriously affects reliability and performance [10–13]. Recently, various studies have been conducted on the modification of the surface and structure of nanocellulose. The modification is mainly based on the reactivity of the hydroxyl group for surface and structural properties. It is through functionalization reactions—such as oxidation, etherification, esterification, silylation, and polymer grafting—that nanocellulose can improve its extraction capacity and enhance the hydrophobicity of its surface [7,14,15].

Hydrophobic surfaces are formed due to the combination of two key factors: low surface energy, and surface roughness (i.e., hierarchical structures). A surface can become superhydrophobic when it is imparted with microroughness or nanoroughness. These surface properties are typically characterized by a water contact angle (WCA) greater than 150° and a sliding angle of less than 10° [16–18]. This can be explained via the Wenzel state [19] and Cassie state [20], using the “lotus” model. The wetting behavior of surfaces has attracted much attention because of its wide range of applications, such as for self-cleaning, anti-icing, water–oil separation, and anticorrosion. These characteristics are also reported in various forms, such as plastic composites, paints, coatings, packaging films, papers, aerogels, and sponges [21–30]. Lu et al. [25] reported magnetic/silanized ethyl cellulose sponges prepared from hexadecyltrimethoxysilane (HDTMS) and mixed with ferroferric oxide (Fe_3O_4) nanoparticles (WCA $> 150^\circ$). Feng et al. [26] reported cellulose/silica aerogels developed from recycled cellulose fibers and methoxytrimethylsilane (MTES), with an average WCA of 151° . Baidya et al. [27] reported superhydrophobic CNF composites fabricated from perfluorooctyltriethoxysilane and [3-(2-aminoethylamino)propyl] trimethoxysilane, with a WCA of 160° . Nevertheless, fluorinated compounds are expensive, and may accumulate and become toxic in organisms and the environment [31,32]. In addition, many well-known studies using HDTMS have been conducted to impart roughness and superhydrophobicity to the surface of silica nanoparticles. Some studies have investigated the hydrophobic surfaces of cotton or wood using a HDTMS-modified silica nanoparticle coating solution [33–38]. Although many previous studies have focused on the phenomenon of imparting hydrophobicity, quantitative analysis of the modification of HDTMS does not provide a sufficient explanation.

In this study, hydrophobic CNF/silica nanocomposites were prepared through the adsorption of silica nanoparticles on the CNFs’ surface and subsequent modification using HDTMS (Figure 1a). We attempted to impart hydrophobicity using HDTMS with a long alkyl group, and precursors such as MTES with a relatively short alkyl group were excluded from the selection because the formation of nanoparticles was dominant [39]. The CNF/silica nanocomposites were prepared via the sol–gel method. The adsorption behavior and silica nanoparticles could be controlled by adjusting the synthesis conditions, such as water and ammonium hydroxide concentrations, and the scale-up process was applied. The introduction of silica nanoparticles increased the surface roughness, surface area, and thermal stability of the nanocomposites (Figure 1b). The HDTMS-modified CNF/silica nanocomposite could be controlled from around 88° to 159° through the HDTMS concentration (with a HDTMS concentration of around 0.1 to 2.0 wt%). In addition, as a result of the hydrolysis–condensation reaction of HDTMS, it was possible to obtain the contents of the thermally decomposed organic region and the non-decomposed inorganic region through TGA. In particular, it was confirmed that the HDTMS-modified CNF/silica nanocomposite (with a HDTMS concentration of ~ 2.0 wt%) had an HDTMS content of ~ 56.18 wt% (inorganic HDTMS 12.24 wt%, organic HDTMS 43.94 wt%), and achieved superhydrophobicity ($>159^\circ$) in various pH solutions (Figure 1c). The obtained HDTMS-modified CNFs and CNF/silica nanocomposites were characterized via Fourier-transform infrared (FTIR) spectroscopy, X-ray photoelectron spectroscopy (XPS), thermogravimetric analysis (TGA), field-emission scanning electron microscopy (FE-SEM), and transmission electron microscopy (TEM). The effects of HDTMS-modified CNFs and CNF/silica nanocomposites on the morphology, wettability, and roughness were investigated by measuring the water contact angles, and via atomic force microscopy (AFM). The results can provide a reference for the adsorption of silica nanoparticles on CNFs and the hydrophobic modification of CNF/silica nanocomposites, as well as expanding their range of eco-friendly coating applications.

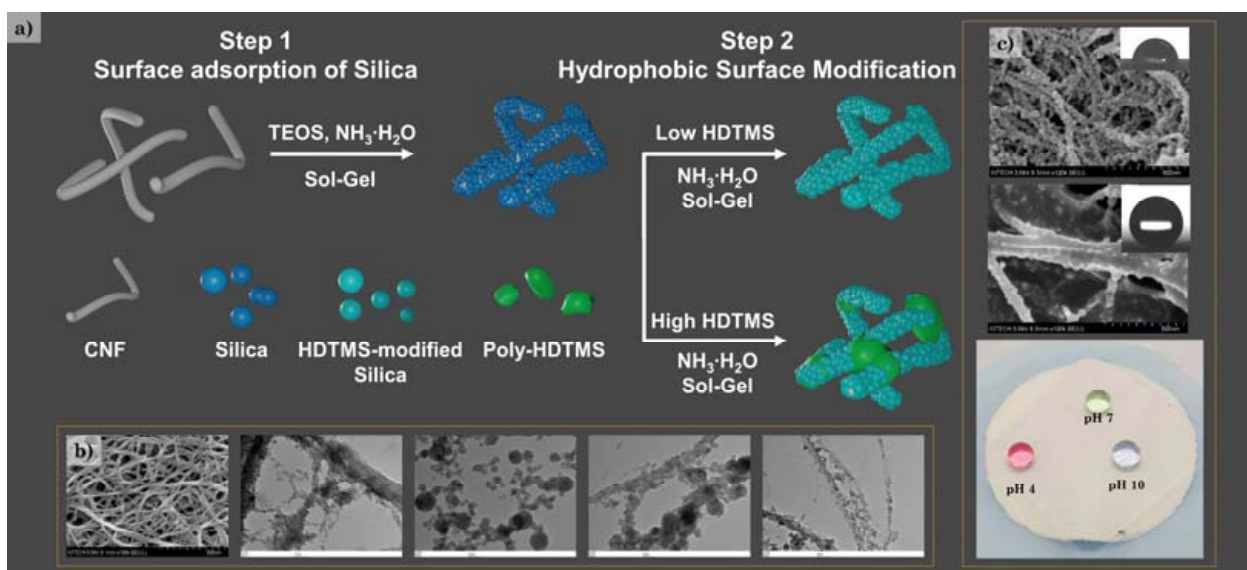


Figure 1. (a) Schematic of the preparation of HDTMS-modified CNF/silica nanocomposites, (b) morphology of CNFs and CNF/silica nanocomposites, and (c) morphology and water droplets on an HDTMS-modified CNF/silica nanocomposite with different pH values.

2. Materials and Methods

2.1. Materials

The CNF dispersion (1 wt%) was purchased from CNNT (Suwon, Korea). The width of the CNFs was in the range of 10–100 nm, and they had a length of several micrometers (Figure S1). The CNFs were manufactured using an aqueous counter collision system, with a fluid containing cellulose fibers that collided with one another at high pressure to fibrillate at the nanoscale. Tetraethyl orthosilicate (TEOS), HDTMS, ammonium hydroxide (NH_4OH , 28 wt%), and ethanol ($\text{CH}_3\text{CH}_2\text{OH}$) were purchased from Sigma-Aldrich (St. Louis, MO, USA).

2.2. Preparation of CNF/Silica, HDTMS-Modified CNF/Silica, and HDTMS-Modified CNF Nanocomposites

In all of these experiments, the CNF dispersion was replaced with ethanol from water. The CNF water dispersion was exchanged via centrifugation dispersion cycles using ethanol. The HDTMS-modified CNF/silica nanocomposites were prepared in two steps by controlling the HDTMS concentration, as shown in Figure 1a. Firstly, the synthesis of the CNF/silica nanocomposite series (CNF/silica-1,2,3, and 4) was examined under different reaction conditions—specifically, by varying the reaction solvent and catalyst concentrations (Table 1). In the first step of the process, ammonium hydroxide was added to the CNF/ethanol solution under stirring and sonication for 15 min. After nitrogen was bubbled at room temperature for at least 30 min to deoxygenate, TEOS was then added at a rate of 2 mL/h. The hydrolysis and condensation reaction was carried out under constant stirring at room temperature for 24 h. After the reaction, the colloid dispersion was purified via centrifugation and redispersion cycles to remove the unreacted precursor and catalyst. Finally, the CNF/silica nanocomposite dispersion was obtained. Secondly, the HDTMS-modified CNF (h-CNF 0.4 and 0.8) and HDTMS-modified CNF/silica nanocomposites (h-sCNF 0.1, 0.5, 1.0, and 2.0) were examined under different HDTMS concentrations (Table 2). HDTMS-modified CNF/silica nanocomposites were prepared using CNF/silica-4 via the sol-gel method at 40 °C. As control samples, HDTMS-modified CNF nanocomposites were also investigated. All samples were purified via several centrifugation and redispersion cycles to remove the unreacted precursor and catalyst. The compositions are shown in Tables 1 and 2.

Table 1. A typical recipe for the preparation of CNF/silica nanocomposites by varying the reaction solvent and catalyst concentrations.

Samples	CNF (g)	TEOS (mL)	EtOH (mL)	NH ₄ OH (mL)	H ₂ O (mL)	$\frac{[H_2O]}{[TEOS]}$	NH ₄ OH (M)
CNF/silica-1	0.20	2.00	95.00	3.00	-	11.96	0.44
CNF/silica-2	0.20	2.00	85.50	3.00	9.50	70.39	0.44
CNF/silica-3	0.20	2.00	87.50	1.00	9.50	62.42	0.15
CNF/silica-4	0.80	4.00	230.00	6.00	-	11.96	0.36

Table 2. A typical recipe for the preparation of CNF/silica, h-CNF, and h-sCNF nanocomposites by varying the HDTMS concentrations.

Samples	CNF (g)	CNF/Silica (g)	TEOS (mL)	HDTMS (mL)	NH ₄ OH (mL)	H ₂ O (mL)
1 Step	CNF/silica	0.8	-	4.0	-	6.0
	h-sCNF 0.1	-	0.5	-	0.1	2.5
2 Step	h-sCNF 0.5	-	0.5	-	0.5	2.5
	h-sCNF 1.0	-	0.5	-	1.0	2.5
	h-sCNF 2.0	-	0.5	-	2.0	2.5
Control	h-CNF 0.4	0.2	-	-	0.4	2.5
	h-CNF 0.8	0.2	-	-	0.8	2.5

2.3. FE-SEM and TEM Analysis

The morphology of the CNF, CNF/silica, h-sCNF, and h-CNF nanocomposites was examined via FE-SEM (SU8020, Hitachi, Tokyo, Japan) and TEM (HT7700, Hitachi, Tokyo, Japan). The FE-SEM images were collected at an accelerating voltage of 3 kV. The samples were coated onto a silicon wafer using a solution of CNF/silica nanocomposites diluted in ethanol; the wafer was then coated with Pt/Pd using an ion sputter coater (E-1045, Hitachi, Tokyo, Japan). The TEM images were collected at an acceleration voltage of 100 kV on a carbon-coated copper grid.

2.4. Zetasizer Analyzer and Zeta Potential Analysis

The Z-average particle size was measured at 25 °C with a Zetasizer (Nano ZS, Malvern Instruments Ltd., Worcester, UK) using a ~0.1% dispersion solution. The zeta potential (ζ) was determined using a laser electrophoresis zeta potential analyzer (Nano ZS, Malvern Instruments Ltd.). The zeta potential analysis was performed at pH 12 and 25 °C. The zeta potential was calculated from the electrophoretic mobility (μ_e) using Smoluchowski's equation,

$$\zeta = \frac{4\pi\eta}{\epsilon} \times \mu_e \quad (1)$$

where ζ is the zeta potential in mV, ϵ is the dielectric constant of the medium, η is the viscosity of the solution, and μ_e is the electrophoretic mobility [40].

2.5. FTIR Spectroscopy and XPS Analysis

The chemical structure and composition of the CNF, CNF/silica, h-sCNF, and h-CNF nanocomposites were characterized via FTIR spectroscopy (Cary 600 Series, Agilent Technologies, Santa Clara, CA, USA) in the range of 4000–600 cm⁻¹, and via XPS (NEXSA, Thermo Fisher, Waltham, MA, USA) with a monochromated Al K α source (1486.6 eV).

2.6. TGA

The thermal properties were measured using a thermogravimetric analyzer (Q500, TA Instruments, New Castle, DE, USA). The silica and the inorganic/organic HDTMS were confirmed by the thermal decomposition amount and residual amount. The measurements

were performed using a weight of 10 ± 0.5 mg to raise the temperature to 800 °C under nitrogen gas.

2.7. WCA and AFM Analysis

The surface properties and WCA were analyzed using a contact angle analyzer (Smart-Drop standard, FEMTOFAB, Seongnam, Korea); the measurements were conducted three times at room temperature with 1 mL water droplets. The surface roughness and morphology of the dimple nanostructures were measured via AFM (NX10, Park Systems, Suwon, Korea) in noncontact mode. The samples were coated onto a PET film by spray-coating.

3. Results and Discussion

3.1. Effect of the Synthesis Conditions on the Morphology of the CNF/Silica Nanocomposites

Figure 2 and Table 3 show the morphology of the CNF/silica nanocomposites obtained using different synthesis conditions—specifically, by varying the reaction solvent and catalyst concentrations. The size of the silica nanoparticles was determined via the TEM image analysis and the Zetasizer analysis, and the silica content was determined via TGA. In the CNF/silica-1, it was confirmed that anisotropic silica nanoparticles with a size of around 10–30 nm were adsorbed on the CNF surface (Figure 2a,b). Butler et al. reported that, under low $[H_2O]/[TEOS]$ molar ratios, a matrix with a more open structure was produced because of incomplete hydrolysis [41]. Increasing the water content of the CNF/silica nanocomposites (CNF/silica-2) resulted in an increase in the silica particle size and the formation of isotropic silica nanoparticles; additionally, the silica content increased from around 57.93 to 70.00 wt% (Figure 2c,d). Decreasing the ammonium hydroxide concentration of the CNF/silica-3 compared to CNF/silica-2 resulted in a decrease in the silica particle size and silica content to ~67.81 wt% (Figure 2e,f). The scale-up process (CNF/silica-4) produced similar results to CNF/silica-1. Indeed, the silica content decreased slightly because the ammonium hydroxide concentration was slightly lower, which can be expected to result in smaller silica nanoparticles. Figure 3 shows the morphology and schematic of the adsorption and separation of silica nanoparticles on the CNF surface. The adsorption of silica nanoparticles was investigated by measuring the zeta potential of CNFs and CNF/silica nanocomposite in ethanol solution at pH 12. The zeta potential of the CNFs and CNF/silica nanocomposite was -31.2 mV and -61.2 mV, respectively. This result shows that both CNFs and CNF/silica nanocomposites are in a stable state in an ethanol solution. In general, the threshold of stability of a colloidal nanoparticle solution in terms of the zeta potential is ± 30 mV [40]. In particular, the CNFs have relatively lower repulsive force between nanofibers than silica nanoparticles. Therefore, the incorporation of silica nanoparticles in the CNFs makes the colloidal solution relatively more stable than CNFs alone. Previous studies have shown that silica nanoparticles are in a relatively more stable state at around -60 mV in a pH solution [42].

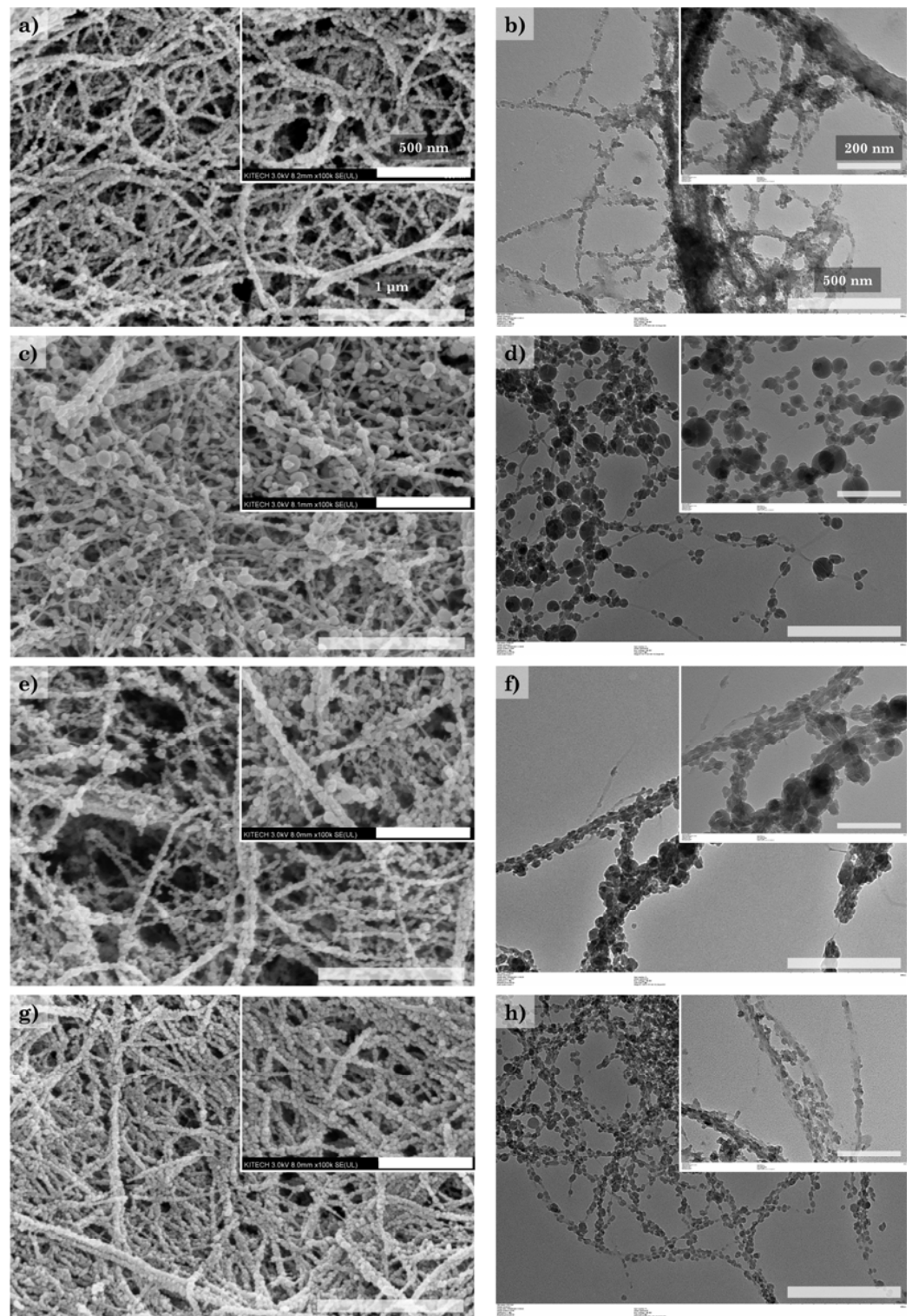


Figure 2. Morphology of CNF/silica nanocomposites investigated via SEM and TEM analysis: (a,b) CNF/silica-1, (c,d) CNF/silica-2, (e,f) CNF/silica-3, and (g,h) CNF/silica-4.

Table 3. Silica particle size and silica content of CNF/silica nanocomposites.

Samples	Particle Size		Silica Content (wt%) (c)
	Size (nm) (a)	Size (nm) (b)	
CNF/silica-1	10 ~ 30	166.1	57.93
CNF/silica-2	13 ~ 90	96.57	70.00
CNF/silica-3	16 ~ 78	57.02	67.81
CNF/silica-4	10 ~ 30	85.07	57.67

(a) Particle size measurement analysis of 30 samples by TEM images, (b) by Zetasizer, and (c) by TGA analysis.

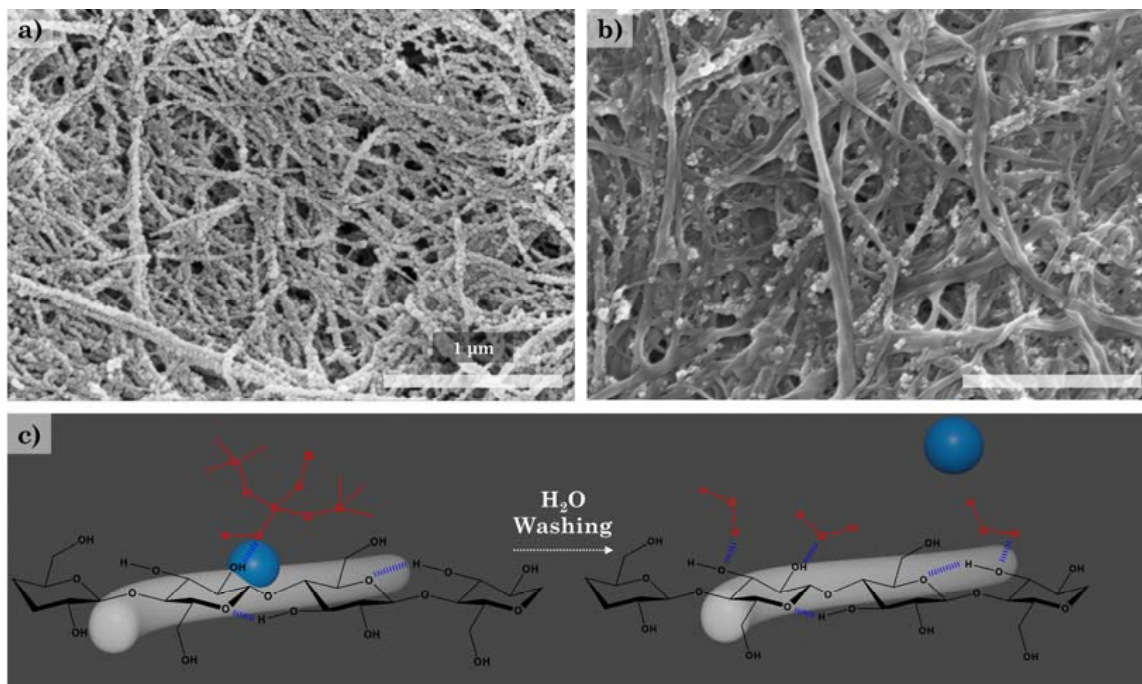


Figure 3. Morphology of the CNF/silica nanocomposites investigated via SEM analysis: (a) CNF/silica-1, (b) CNF/silica-1 after washing with water, and (c) scheme of adsorption and separation of silica nanoparticles on the CNFs' surface.

The addition of water with relatively strong hydrogen bonding results in the separation between silica nanoparticles and CNFs. It is considered that the affinity between CNFs and water is relatively higher than that of silica nanoparticles. Similarly, in other studies, it can be seen that CNFs have a high affinity for water, with a zeta potential of around -65 mV [43,44].

As a result, the adsorption of the silica nanoparticles on the CNF surface appears to be a phenomenon that occurs due to hydrogen bonding rather than covalent bonding. Additionally, the adsorbed silica nanoparticles were separated from the water solution using ultrasonic waves, and the silica nanoparticle size was measured using a Zetasizer. The size of silica nanoparticles in CNF/silica-1 was ~ 166 nm, while that in CNF/silica-4 was ~ 85 nm, showing rather large values, unlike TEM analysis. It is expected that anisotropic silica nanoparticles are actually agglomerated with one another. In particular, the difference in the silica nanoparticle size of CNF/silica-4 compared to CNF/silica-1 was thought to be due to the relatively high CNF concentration (0.20% to 0.33%) and low TEOS concentration (2.00% to 1.67%). As a result, the size and content of the silica nanoparticles can be controlled through water and ammonium hydroxide concentrations. In a previous work, it was found that increasing the water content resulted in an increase in the silica particle size and a decrease in the packing efficiency. Silica nanoparticles are generated and stabilized in an excess of an aqueous solution, which decreases their adsorption on the CNF surface [42].

3.2. Chemical Structure of the CNF, CNF/Silica, HDTMS-Modified CNF/Silica, and HDTMS-Modified CNF Nanocomposites

Figure 4 shows the FTIR spectra of the CNF, CNF/silica, HDTMS-modified CNF/silica, and HDTMS-modified CNF nanocomposites. The absorption peaks of the CNF/silica nanocomposites are attributed to the Si–OH and Si–O–Si vibration in the range 3100–3500 cm^{-1} , as well as at 1080 and 800 cm^{-1} [42,45,46]. The absorption peaks at 3100–3500 and 1080 cm^{-1} partially overlap with the CNF absorption peak, and tend to shift toward slightly higher wavelengths. Modification with HDTMS yielded additional absorption peaks at 2925, 2845, and 1458 cm^{-1} , which were attributed to the $-\text{CH}_2\text{CH}_2$ and $-\text{CH}_3$ vibrations of the alkyl group ($-\text{C}_{16}\text{H}_{33}$) [36]. In Figure 4, the highlighted area represents the integral values of the spectra of the alkyl group (3038–2788 cm^{-1} , and 1410–1400 cm^{-1}) and the silane group (863–740 cm^{-1}). Increasing the HDTMS concentration in CNF/silica nanocomposites increases the peak area of the alkyl group compared with that of the silane group. In h-sCNF 0.1, the peak of the alkyl group did not appear clearly, but the peak areas increased slightly from around 0.38 to 0.47 (3038–2788 cm^{-1}) and from 0.10 to 0.15 (1419–1400 cm^{-1}); therefore, it was inferred that a sufficient HDTMS modification had occurred. Similarly, the HDTMS modification of the CNF nanocomposites resulted in the appearance of peaks attributed to the alkyl group.

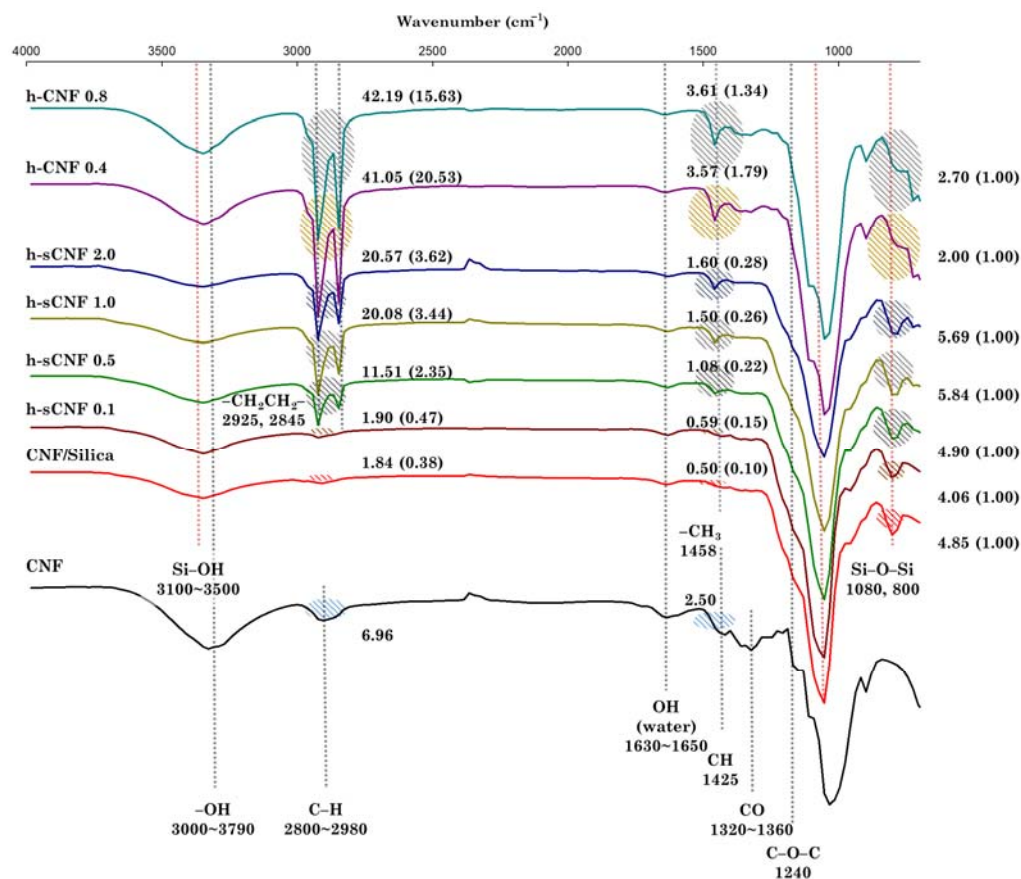


Figure 4. FTIR spectra of the CNF, CNF/silica, h-sCNF, and h-CNF nanocomposites in the range of 4000–600 cm^{-1} , and measured absorption peak areas of the alkyl group (3038–2788, 1419–1400 cm^{-1}) and the silane group (863–740 cm^{-1}).

3.3. Characterization of the CNF, CNF/Silica, HDTMS-Modified CNF/Silica, and HDTMS-Modified CNF Nanocomposites

Table 4 and Figure 5 show the elemental composition of the CNF surface before and after modification with TEOS and HDTMS, as investigated via XPS. CNFs predominantly consist of C (56.20%) and O (43.80%), which is consistent with the $(\text{C}_6\text{H}_{10}\text{O}_5)_n$ composition of cellulose. The calculations of the amounts of CNFs, silica, and HDTMS are presented

in the Supplementary Materials. Here, the amount of HDTMS was calculated assuming $\text{CH}_3(\text{CH}_2)_{15}\text{SiO}_k$ ($k = 1$). In the CNF/silica nanocomposites, silica nanoparticles showed surface adsorption of ~55.15 wt% to the mass of the CNFs. As the concentration of HDTMS increased, the HDTMS modification of the CNF/silica nanocomposites increased from ~8.17 wt% to ~56.18 wt%, whereas the HDTMS modification of the CNF nanocomposites decreased from ~39.46 wt% to ~34.73 wt%. The results show a similar trend to the FTIR analysis.

Table 4. Surface composition of the CNF, CNF/silica, h-sCNF, and h-CNF nanocomposites, as measured via XPS.

Samples	Atomic Percentage (%)			Amount (%)			FWHM
	C	O	Si	CNF	Silica	HDTMS	
CNF	56.20	43.80	-	100.00	-	-	-
CNF/silica	29.20	54.65	16.15	44.85	55.15	-	1.96
h-sCNF 0.1	33.94	50.97	15.05	40.65	51.18	8.17	1.98
h-sCNF 0.5	52.82	35.78	11.40	30.14	34.04	35.82	2.11
h-sCNF 1.0	57.14	31.85	11.01	24.98	31.09	43.92	2.18
h-sCNF 2.0	64.82	25.66	9.52	20.29	23.53	56.18	2.37
h-CNF 0.4	67.30	30.55	2.15	60.53	-	39.46	1.82
h-CNF 0.8	66.71	31.37	1.92	65.27	-	34.73	1.76

As shown in Figure 5a–d, the high-resolution C1s spectra of the samples were fitted with three peaks—namely, C1, C2, and C3 at 284.3 ± 0.1 , 286.0 ± 0.2 , and 287.4 ± 0.3 eV, respectively, which correspond to the C–C/C–H/C–Si, C–O/C–OH, and O–C–O/C=O groups, respectively [47]. As shown in Figure 5e–k, the high-resolution Si2p spectra of the samples were fitted with three peaks—namely, S1, S2, and S3 at 102.0 ± 0.2 , 102.9 ± 0.1 , and 103.5 ± 0.1 eV, respectively, which correspond to the Si–C and SiO₂ groups [47–49]. For Si2p spectra, the chemical structure was observed with binding energies of 102.9 eV and 103.5 eV corresponding to the Si oxidation states Si³⁺ and Si⁴⁺, respectively [48,50–52]. As shown in Figure 5a–d, the HDTMS modification of the CNF/silica nanocomposites resulted in an increase in the C1 peak (284.4 eV) and a significant decrease in the C2 (286.0 eV) and C3 (287.4 eV) peaks for oxygen-containing groups.

Similarly, the C1 peak is pronounced in h-CNF (Figure 5c,d), but it is difficult to find a trend for the HDTMS concentration. As shown in Figure 5e–h,j,k, the new peak corresponding to S1 (102.0 eV) gradually increases in the h-sCNF nanocomposites, thus showing a trend of increasing full width at half-maximum (FWHM) from 1.95 (CNF/silica) to 2.37. The h-CNF nanocomposites exhibit binding energy of S1 (102.0 eV) and S2 (102.9 eV) [48,49]; as a result, the appearance of new peaks corresponding to C1 (284.3 eV) and S1 (102.0 eV) indicates that the Si–C groups were introduced in the CNF and CNF/silica nanocomposites. In particular, the HDTMS modification at high concentrations for the CNF (h-CNF 0.8) nanocomposites results in a reduction in the S2 (103.0 eV) peak of SiO₂ compared to the h-CNF 0.4 (Figure 5j,k); that is, in h-CNF 0.4, the SiO₂ structure is considered to be relatively more dominant than in h-CNF 0.8. This part will be dealt with in more detail in the TGA and morphological analysis.

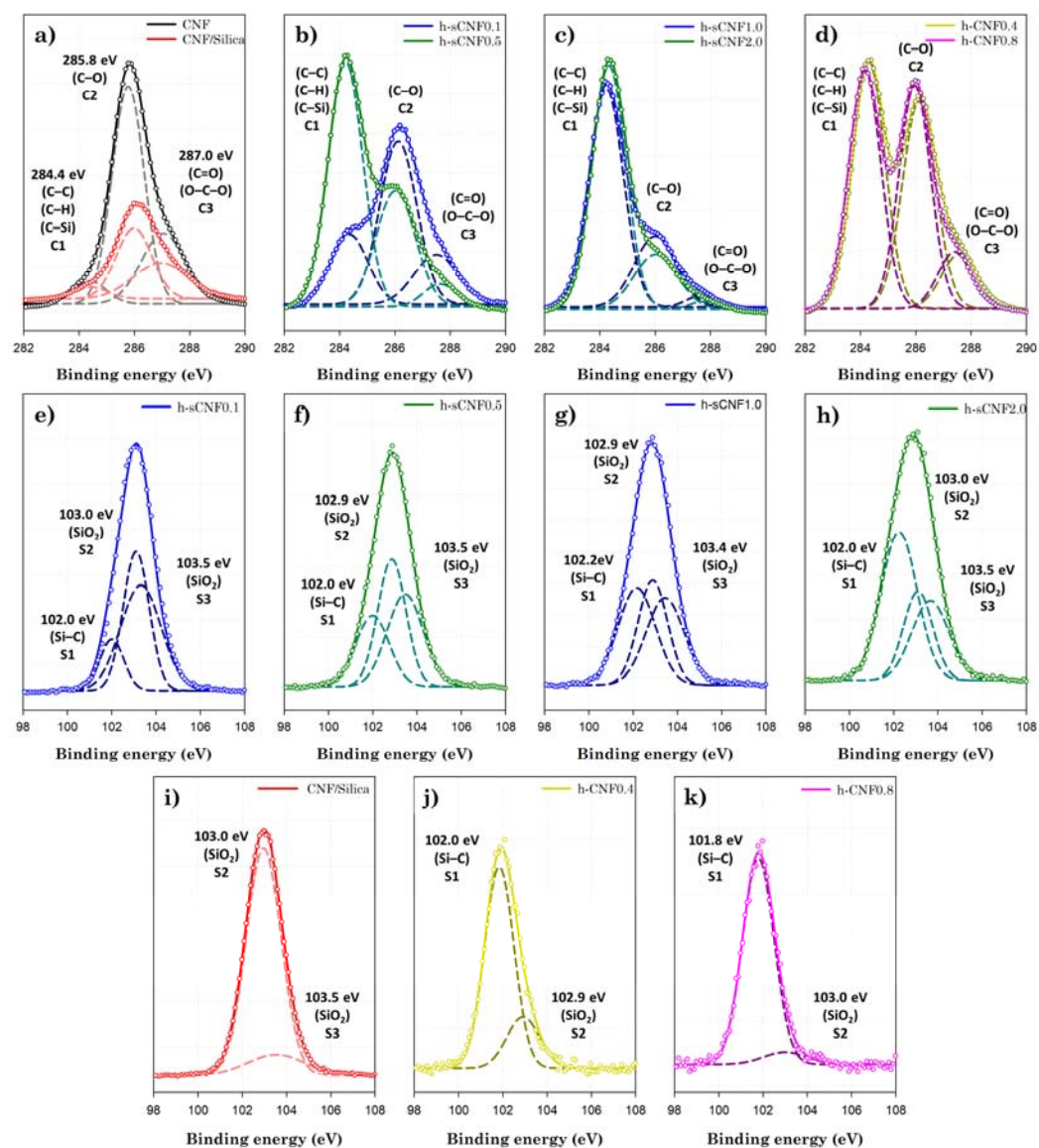


Figure 5. Chemical composition of the CNF, CNF/silica, h-sCNF, and h-CNF nanocomposites, as investigated via XPS: (a–d) high-resolution C1s, and (e–k) high-resolution Si 2p peak.

3.4. Thermal Degradation Properties of the CNF, CNF/Silica, HDTMS-Modified CNF/Silica, and HDTMS-Modified CNF Nanocomposites

Figure 6 shows the TGA and derivative thermogravimetric (DTG) curves of the CNF, CNF/silica, HDTMS-modified CNF/silica, and HDTMS-modified CNF nanocomposites. Table 5 summarizes the thermal degradation properties (T_{10} , $T_{inf,1}$, $T_{inf,2}$, and T_{max}) of the CNFs, silica, and inorganic/organic HDTMS. The inorganic/organic component content of HDTMS was calculated based on the results of the TGA and XPS analysis. The calculation is shown in detail in the Supplementary Materials. The CNFs mainly exhibited first-order degradation (D_{1st}) in the range from around 220 °C to 420 °C, and then almost degradation at a temperature exceeding 670 °C as second-order degradation (D_{2nd}). The amorphous and crystalline components were found to be ~74.09 wt%, the total degradation of the crystalline cellulose polymer chain was ~25.03 wt%, and the remainder was ~0.88 wt% of ash. Such values are similar to those reported for the thermal decomposition of cellulose obtained from other plant sources [53], due to the different binding energies of the chemical structure and crystallinity [53–55]. The T_{10} and $T_{inf,1}$ of the CNFs were around 311.23 °C and 346.87 °C, respectively. CNF/silica nanocomposites tended to increase to around 337.64 °C and 357.39 °C. The thermal stability of the silica nanoparticles was mainly due to the three-

dimensional network structure of SiO₂. Generally, the incorporation of inorganic materials into the polymer matrix can enhance thermal stability by acting as a superior insulator and mass transport barrier to the volatile products generated during decomposition [56,57]. Additionally, the volatilization of the CNFs may decrease because of the labyrinth effect of the silica nanoparticles [58,59]. This effect is expected to increase the ash content in the CNF nanocomposites from 0.88 wt% to 2.26 wt%. Similarly, the HDTMS modification gives rise to inorganic/organic HDTMS, and the inorganic composition serves to improve the thermal stability as an insulator does. In particular, HDTMS-modified CNF/silica nanocomposites have decreased inorganic content (silica and inorganic HDTMS) compared to CNF/silica, but increased T_{10} and $T_{inf,1}$, because organic HDTMS exhibits high thermal stability at a decomposition temperature from around 519 °C to 527 °C [60–63].

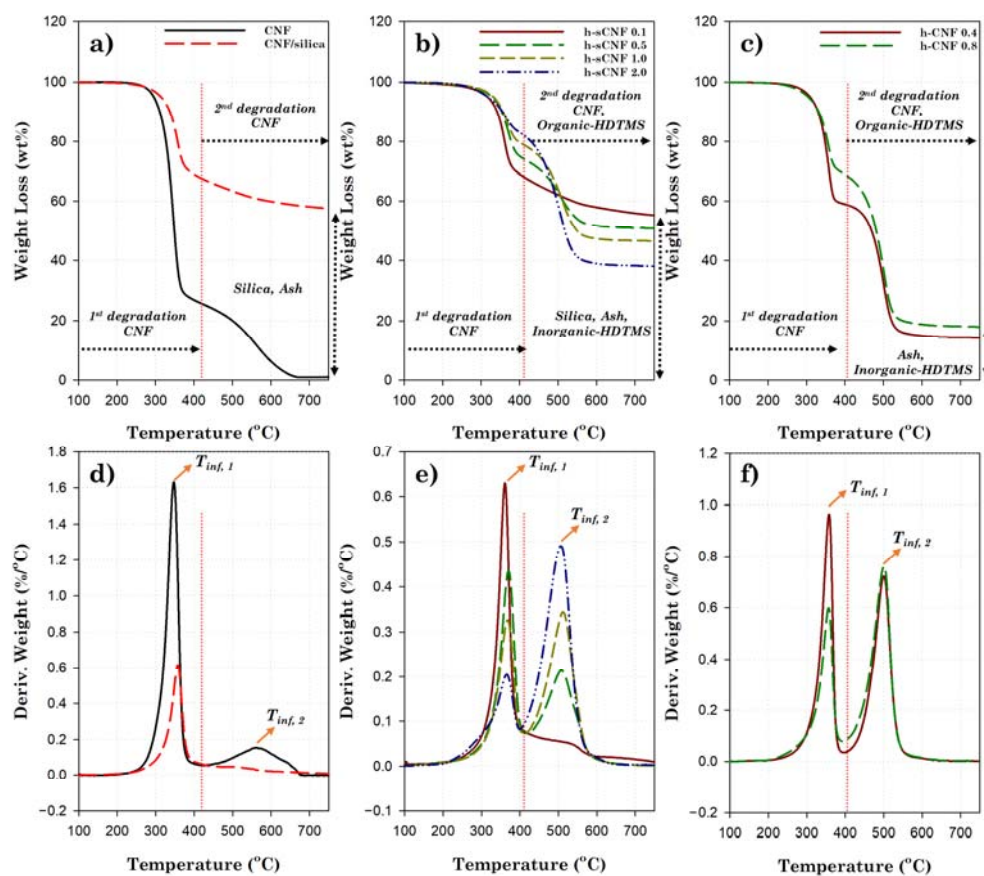


Figure 6. TGA and DTG curves of the CNF, CNF/silica, h-sCNF, and h-CNF nanocomposites: (a,d) CNF and CNF/silica, (b,e) h-sCNF, and (c,f) h-CNF nanocomposites.

Table 5. Thermal degradation properties (T_{10} , $T_{inf,1}$, $T_{inf,2}$, and T_{max}) of the CNF, CNF/silica, h-sCNF, and h-CNF nanocomposites, and inorganic/organic component content of HDTMS for the h-CNF and h-sCNF nanocomposites.

Samples	T_{10} (°C)	^a $T_{inf,1}$ (°C)	^a $T_{inf,2}$ (°C)	^b T_{max} (wt%)	Inorganic HDTMS (wt%)	Organic HDTMS (wt%)
CNF	311.23	346.87	560.01	0.88	-	-
CNF/silica	337.64	357.39	-	57.41	-	-
h-sCNF 0.1	341.63	360.87	-	55.02	1.58	6.59
h-sCNF 0.5	353.85	370.49	508.44	50.77	14.47	21.35
h-sCNF 1.0	357.16	367.86	512.58	46.54	13.19	30.73
h-sCNF 2.0	355.69	365.05	506.00	38.03	12.24	43.94
h-CNF 0.4	329.88	357.91	500.05	14.34	13.46	26.00
h-CNF 0.8	331.74	356.59	500.82	17.93	17.05	17.68

^a: Inflection point of the TGA curve; ^b: residual amount.

The HDTMS decomposed in a wide temperature range of ~200–500 °C, due to the relatively insufficient Si–O–Si crosslinking structure and the organic region of the hexadecyl group ($-\text{CH}_2(\text{CH}_2)_{14}\text{CH}_3$) [33,38,64,65]. Figure S2 shows the differential scanning calorimetry (DSC) curve of the CNF/silica and HDTMS-modified CNF/silica nanocomposites. A melting temperature of ~44.76 °C was confirmed via the DSC analysis, proving that organic HDTMS was produced. Increasing the HDTMS concentration of the CNF/silica nanocomposites gradually increased the organic HDTMS content but slightly decreased the inorganic HDTMS content; therefore, the h-sCNF 1.0 and h-sCNF 2.0, which had relatively high organic content, exhibited a slight decrease in thermal stability compared to h-sCNF 0.5. However, increasing the HDTMS concentration of the CNF nanocomposites resulted in a decrease in the organic HDTMS content from around 26.00 wt% to 17.68 wt%. It can be seen that this is consistent with the trend of the previous FTIR and XPS analyses.

3.5. Surface Properties of the CNF, CNF/Silica, HDTMS-Modified CNF/Silica, and HDTMS-Modified CNF Nanocomposites

Figure 7 shows SEM and TEM images used to examine the modification of CNFs with HDTMS in more detail. Modification of the CNF nanocomposites at a low HDTMS concentration (h-CNF 0.4) results in the formation of HDTMS particles (Figure 7a,c). On the other hand, in h-CNF 0.8, a coating can be observed on the CNF surface, and the HDTMS particles are seldom observed (Figure 7b,d). It was expected that the HDTMS particles would be formed simultaneously with the coating of the CNF surface in the modification process. In particular, h-CNF 0.8 is probably due to the presence of a uniform coating on the CNF surface, which forms a hydrophobic surface, and the HDTMS particles are easily removed during the washing process. Therefore, h-CNF 0.8 shows a relatively lower HDTMS content than h-CNF 0.4 and, in particular, the organic HDTMS content is significantly reduced. These results are expected to show limitations in the modification with HDTMS due to the low surface area of the CNFs. Figure 8 shows the morphology of the HDTMS-modified CNF/silica nanocomposites with different HDTMS concentrations. Increasing the HDTMS concentration gradually increases the coating area on the CNF/silica nanocomposites. h-sCNF 2.0 is coated on the entire surface. Many studies have reported the HDTMS modification of the surface of silica nanoparticles. Chang et al. [35,36] reported that the silica nanoparticles were connected by a polymeric bridge, indicating a clear tendency to aggregate with one another. At a low HDTMS concentration, the surface of the silica nanoparticles became fuzzy, and tended to be coated with a thin layer. At a high HDTMS concentration, the silica particles were densely coated with the polymer to form a core-shell structure. Chang et al. [35] reported that an extremely dense polymer network was observed at an HDTMS concentration of 5%.

The WCAs were investigated to examine the hydrophobicity of the HDTMS-modified CNF nanocomposites. As shown in Figure 9a, the CNF and CNF/silica nanocomposites exhibited low water repellency, with a WCA of around 4.5° and 35.9°, respectively. The HDTMS-modified CNF nanocomposites exhibited water repellency, with a WCA of ~79.3°, and the HDTMS-modified CNF/silica nanocomposites showed high water repellency, with a WCA of ~159.1°. The HDTMS of h-CNF 0.4 and 0.8 was around 39.46 wt% and 34.73 wt%, respectively, whereas in h-sCNF 0.5 it was ~35.82 wt%, indicating high WCA despite similar or lower content. In particular, h-sCNF 2.0 exhibited superhydrophobicity, with a WCA of ~159.1°. This sample also exhibited superhydrophobicity in various aqueous solutions with different pH values (Figure 9b); this was mainly attributed to the hydrophobicity of the long alkyl chain of HDTMS. In addition, the incorporation of silica nanoparticles increased the roughness of the surface, thereby remarkably improving its water repellency.

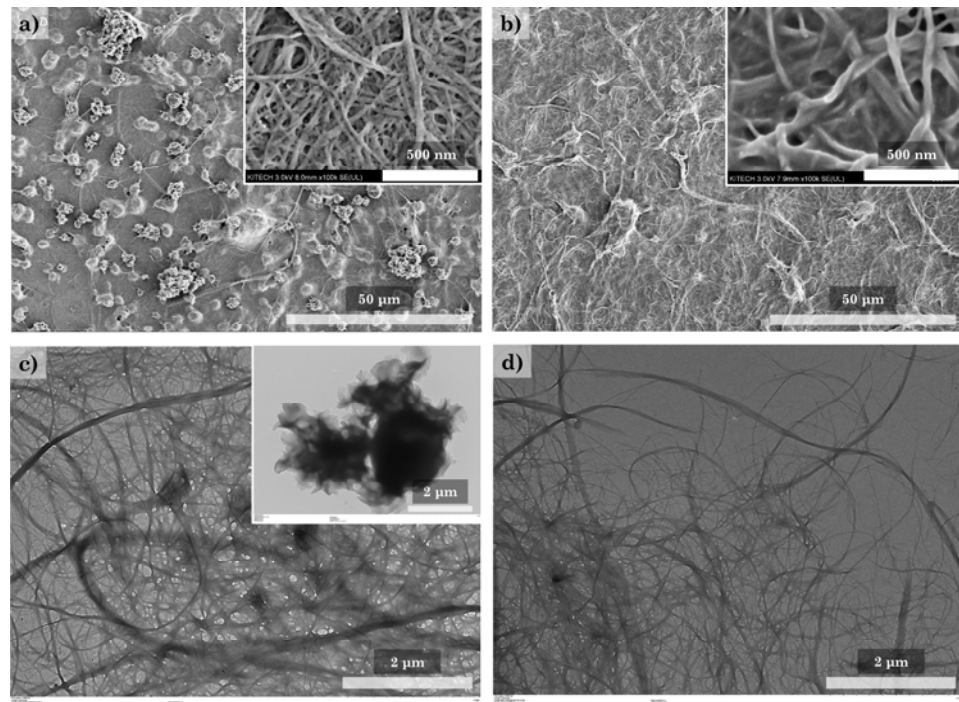


Figure 7. Morphology of the HDTMS-modified CNF nanocomposites, observed via SEM and TEM analysis: (a,c) h-CNF 0.4 and (b,d) h-CNF 0.8.

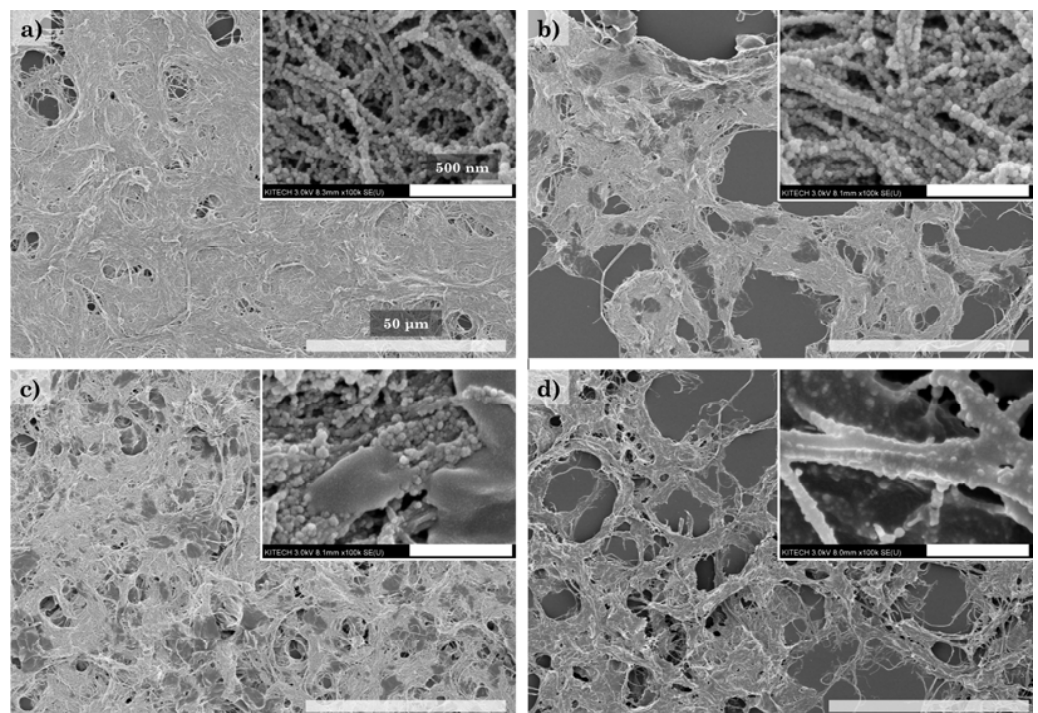


Figure 8. Morphology of the HDTMS-modified CNF/silica nanocomposites, observed via SEM analysis: (a) h-sCNF 0.1, (b) h-sCNF 0.5, (c) h-sCNF 1.0, and (d) h-sCNF 2.0.

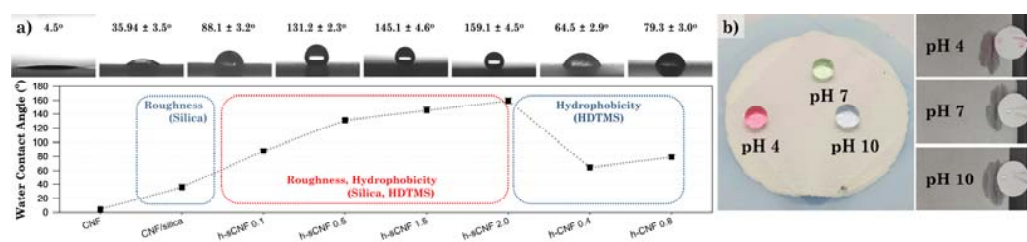


Figure 9. (a) Surface properties of the CNF, CNF/silica, h-sCNF, and h-CNF nanocomposites obtained via contact angle analysis. (b) Water droplets with pH values of 4, 7, and 10 exhibited a spherical shape on the surface.

As shown in Figure 10, the roughness values of each sample were examined via AFM. The CNF and HDTMS-modified CNF nanocomposites showed a smooth surface, with roughness values of around 49.67 nm, 36.65 nm, and 32.21 nm. The reason for the decreases in the roughness was that the roughness decreased due to the HDTMS coating on the CNF surface. On the other hand, the CNF/silica and HDTMS-modified CNF/silica nanocomposites showed relatively rough surfaces, with roughness values ranging from around 112.21 to 134.53 nm. These results show the effect that the incorporation of silica nanoparticles in the CNFs imparts nanoroughness. In addition, it was confirmed that the increase in HDTMS content imparted microroughness to HDTMS-modified CNF/silica nanocomposites by aggregating CNFs with one another (Figure 8). Similarly, many studies have reported the possibility to impart roughness and superhydrophobicity to the surface of silica particles using HDTMS [33–37,66]. Xu et al. [34] reported that the change in hydrophobicity was not significant when the HDTMS concentration was higher than 2%. Chang et al. [35] showed that a HDTMS concentration of 1 wt% is the most optimal. However, the hydrophobicity does not increase further with a higher HDTMS concentration, because the hierarchical structure features derived from the silica particles are hidden in the dense network of the coating; consequently, the roughness is no longer improved. Therefore, the HDTMS-modified CNF nanocomposites have limitations in terms of imparting hydrophobicity. On the other hand, the incorporation of silica nanoparticles into CNFs was more beneficial for the HDTMS modification; as a result, the content of organic HDTMS was increased. In addition, it is expected that a more pronounced surface modification of HDTMS may be possible due to the increased surface area.

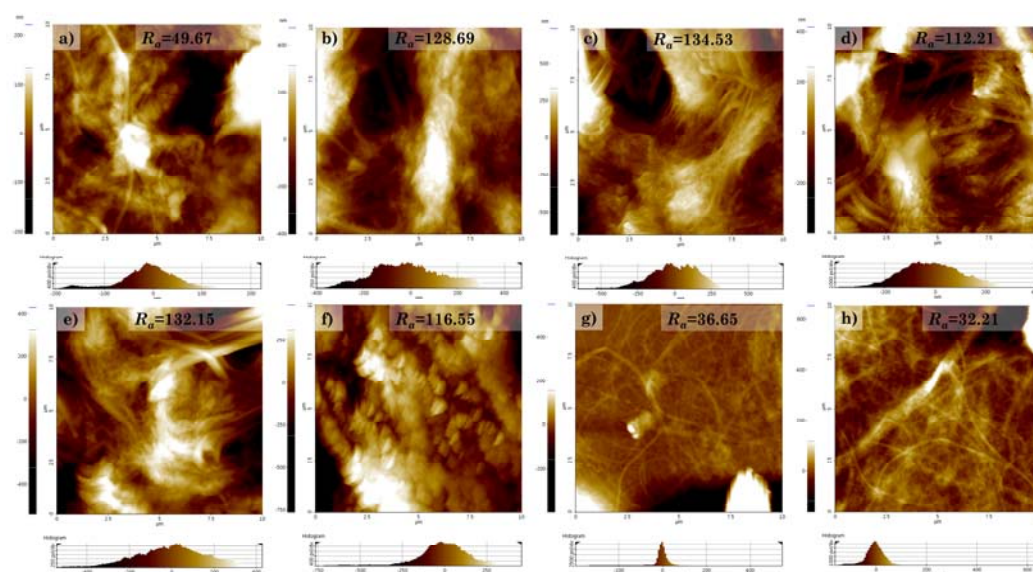


Figure 10. Surface roughness imaged via AFM ($10 \mu\text{m} \times 10 \mu\text{m}$ image): (a) CNF, (b) CNF/silica, (c) h-sCNF 0.1, (d) h-sCNF 0.5, (e) h-sCNF 1.0, (f) h-sCNF 2.0, (g) h-CNF 0.4, and (h) h-CNF 0.8.

4. Conclusions

Firstly, we controlled the adsorption behavior of silica nanoparticles on the surface of CNFs by adjusting the synthesis conditions. The silica nanoparticles' size and the packing efficiency of the CNF surface could be controlled by varying the concentrations of ammonium hydroxide and water. Increasing the water and ammonium hydroxide concentrations increased the particle size of isotropic silica nanoparticles, while decreasing the concentration decreased the particle size of anisotropic silica nanoparticles. The incorporation of silica nanoparticles could impart thermal stability and surface roughness to the CNFs. The degradation temperature increased from around 311.23 °C and 346.87 °C to 337.64 °C and 357.39 °C, while the surface roughness increased from around 49.67 to 128.69. Above all, the phenomenon in which silica nanoparticles adsorbed on CNFs are desorbed again via a water-based solution has the potential to be applied to fields where recycling is easy.

Secondly, we successfully grafted HDTMS onto the surface of CNF and CNF/silica nanocomposites. The behavior of modified HDTMS was quantitatively analyzed via FTIR, XPS, TGA, SEM, and TEM. HDTMS modification could increase the thermal stability more effectively through the incorporation of silica nanoparticles, and imparted additional hydrophobicity. The HDTMS-modified CNF/silica nanocomposites could be controlled from around 88° to 159° through the HDTMS concentration. In particular, h-sCNF 2.0 exhibited superhydrophobicity, with a WCA of ~159.1° in various aqueous solutions with different pH values. This study can provide a reference for the adsorption of silica nanoparticles and the hydrophobic modification of CNF nanocomposites, as well as expand their fields of application.

Supplementary Materials: The following supporting information can be downloaded at <https://www.mdpi.com/article/10.3390/polym14040833/s1>, Figure S1: Morphology of the CNFs investigated via (a) SEM and (b) TEM; Figure S2: DSC curves of the CNF/silica and HDTMS-modified CNF/silica nanocomposites; Table S1: Surface composition of the samples measured via XPS; Table S2: Thermal degradation properties (T_{max}) and amounts of the CNFs, silica, and inorganic/organic HDTMS.

Author Contributions: Conceptualization, G.-H.K. and J.-K.S.; methodology, G.-H.K. and B.-N.J.; software, G.-H.K., B.-N.J., and D.-H.K.; validation, G.-H.K. and J.-K.S.; formal analysis, G.-H.K.; investigation, G.-H.K. and D.-H.K.; writing—original draft preparation, G.-H.K.; writing—review and editing, D.-H.K. and J.-K.S.; project administration, J.-K.S. All authors have read and agreed to the published version of the manuscript.

Funding: This research was part of the project titled “Development to solve current issues in seafood distribution (Project number: 1525011894)”, funded by the Ministry of Oceans and Fisheries, Korea.

Institutional Review Board Statement: Not applicable.

Informed Consent Statement: Not applicable.

Data Availability Statement: Not applicable.

Conflicts of Interest: The authors declare no conflict of interest.

References

1. Khalil, H.A.; Bhat, A.; Yusra, A.I. Green composites from sustainable cellulose nanofibrils: A review. *Carbohydr. Polym.* **2012**, *87*, 963–979. [[CrossRef](#)]
2. Kim, J.-H.; Shim, B.S.; Kim, H.S.; Lee, Y.-J.; Min, S.-K.; Jang, D.; Abas, Z.; Kim, J. Review of nanocellulose for sustainable future materials. *Int. J. Precis. Eng. Manuf. Green Technol.* **2015**, *2*, 197–213. [[CrossRef](#)]
3. Kargarzadeh, H.; Ahmad, I.; Thomas, S.; Dufresne, A. *Handbook of Nanocellulose and Cellulose Nanocomposites*; Wiley Online Library: Hoboken, NJ, USA, 2017.
4. Dufresne, A. Nanocellulose: A new ageless bionanomaterial. *Mater. Today* **2013**, *16*, 220–227. [[CrossRef](#)]
5. Muid Julkapli, N.; Bagheri, S. Nanocellulose as a green and sustainable emerging material in energy applications: A review. *Polym. Adv. Technol.* **2017**, *28*, 1583–1594. [[CrossRef](#)]
6. Lavoine, N.; Desloges, I.; Dufresne, A.; Bras, J. Microfibrillated cellulose—Its barrier properties and applications in cellulosic materials: A review. *Carbohydr. Polym.* **2012**, *90*, 735–764. [[CrossRef](#)]

7. Moon, R.J.; Martini, A.; Nairn, J.; Simonsen, J.; Youngblood, J. Cellulose nanomaterials review: Structure, properties and nanocomposites. *Chem. Soc. Rev.* **2011**, *40*, 3941–3994. [[CrossRef](#)]
8. Abitbol, T.; Rivkin, A.; Cao, Y.; Nevo, Y.; Abraham, E.; Ben-Shalom, T.; Lapidot, S.; Shoseyov, O. Nanocellulose, a tiny fiber with huge applications. *Curr. Opin. Biotechnol.* **2016**, *39*, 76–88. [[CrossRef](#)]
9. Nechyporchuk, O.; Belgacem, M.N.; Bras, J. Production of cellulose nanofibrils: A review of recent advances. *Ind. Crops Prod.* **2016**, *93*, 2–25. [[CrossRef](#)]
10. Lindh, E.L.; Terenzi, C.; Salmén, L.; Furo, I. Water in cellulose: Evidence and identification of immobile and mobile adsorbed phases by 2 H MAS NMR. *Phys. Chem. Chem. Phys.* **2017**, *19*, 4360–4369. [[CrossRef](#)]
11. Zhao, H.; Chen, Z.; Du, X.; Chen, L. Contribution of different state of adsorbed water to the sub-Tg dynamics of cellulose. *Carbohydr. Polym.* **2019**, *210*, 322–331. [[CrossRef](#)]
12. Meriçer, Ç.; Minelli, M.; Baschetti, M.G.; Lindström, T. Water sorption in microfibrillated cellulose (MFC): The effect of temperature and pretreatment. *Carbohydr. Polym.* **2017**, *174*, 1201–1212. [[CrossRef](#)] [[PubMed](#)]
13. Kulasinski, K.; Guyer, R.; Keten, S.; Derome, D.; Carmeliet, J. Impact of moisture adsorption on structure and physical properties of amorphous biopolymers. *Macromolecules* **2015**, *48*, 2793–2800. [[CrossRef](#)]
14. Patel, D.K.; Dutta, S.D.; Lim, K.-T. Nanocellulose-based polymer hybrids and their emerging applications in biomedical engineering and water purification. *RSC Adv.* **2019**, *9*, 19143–19162. [[CrossRef](#)]
15. Thakur, V.; Guleria, A.; Kumar, S.; Sharma, S.; Singh, K. Recent advances in nanocellulose processing, functionalization and applications: A review. *Mater. Adv.* **2021**, *2*, 1872–1895. [[CrossRef](#)]
16. Onda, T.; Shibuichi, S.; Satoh, N.; Tsujii, K. Super-water-repellent fractal surfaces. *Langmuir* **1996**, *12*, 2125–2127. [[CrossRef](#)]
17. Wang, S.; Liu, K.; Yao, X.; Jiang, L. Bioinspired surfaces with superwettability: New insight on theory, design, and applications. *Chem. Rev.* **2015**, *115*, 8230–8293. [[CrossRef](#)] [[PubMed](#)]
18. Wang, S.; Jiang, L. Definition of superhydrophobic states. *Adv. Mater.* **2007**, *19*, 3423–3424. [[CrossRef](#)]
19. Wenzel, R.N. Resistance of solid surfaces to wetting by water. *Ind. Eng. Chem.* **1936**, *28*, 988–994. [[CrossRef](#)]
20. Cassie, A.; Baxter, S. Wettability of porous surfaces. *Trans. Faraday Soc.* **1944**, *40*, 546–551. [[CrossRef](#)]
21. Phanthong, P.; Reubroycharoen, P.; Hao, X.; Xu, G.; Abudula, A.; Guan, G. Nanocellulose: Extraction and application. *Carbon Resour. Convers.* **2018**, *1*, 32–43. [[CrossRef](#)]
22. Lee, K.-Y.; Aitomäki, Y.; Berglund, L.A.; Oksman, K.; Bismarck, A. On the use of nanocellulose as reinforcement in polymer matrix composites. *Compos. Sci. Technol.* **2014**, *105*, 15–27. [[CrossRef](#)]
23. Cai, J.; Liu, S.; Feng, J.; Kimura, S.; Wada, M.; Kuga, S.; Zhang, L. Cellulose–silica nanocomposite aerogels by in situ formation of silica in cellulose gel. *Angew. Chem.* **2012**, *124*, 2118–2121. [[CrossRef](#)]
24. Shi, J.; Lu, L.; Guo, W.; Zhang, J.; Cao, Y. Heat insulation performance, mechanics and hydrophobic modification of cellulose–SiO₂ composite aerogels. *Carbohydr. Polym.* **2013**, *98*, 282–289. [[CrossRef](#)] [[PubMed](#)]
25. Lu, Y.; Wang, Y.; Liu, L.; Yuan, W. Environmental-friendly and magnetic/silanized ethyl cellulose sponges as effective and recyclable oil-absorption materials. *Carbohydr. Polym.* **2017**, *173*, 422–430. [[CrossRef](#)]
26. Feng, J.; Le, D.; Nguyen, S.T.; Nien, V.T.C.; Jewell, D.; Duong, H.M. Silica cellulose hybrid aerogels for thermal and acoustic insulation applications. *Colloids Surf. A Physicochem. Eng. Asp.* **2016**, *506*, 298–305. [[CrossRef](#)]
27. Baidya, A.; Ganayee, M.A.; Jakka Ravindran, S.; Tam, K.C.; Das, S.K.; Ras, R.H.; Pradeep, T. Organic solvent-free fabrication of durable and multifunctional superhydrophobic paper from waterborne fluorinated cellulose nanofiber building blocks. *ACS Nano* **2017**, *11*, 11091–11099. [[CrossRef](#)]
28. Zou, Y.; Zhao, J.; Zhu, J.; Guo, X.; Chen, P.; Duan, G.; Liu, X.; Li, Y. A mussel-inspired polydopamine-filled cellulose aerogel for solar-enabled water remediation. *ACS Appl. Mater. Interfaces* **2021**, *13*, 7617–7624. [[CrossRef](#)]
29. Deeksha, B.; Sadanand, V.; Hariram, N.; Rajulu, A.V. Preparation and properties of cellulose nanocomposite fabrics with in situ generated silver nanoparticles by bioreduction method. *J. Bioresour. Bioprod.* **2021**, *6*, 75–81. [[CrossRef](#)]
30. Fatima, A.; Yasir, S.; Khan, M.S.; Manan, S.; Ullah, M.W.; Ul-Islam, M. Plant extract-loaded bacterial cellulose composite membrane for potential biomedical applications. *J. Bioresour. Bioprod.* **2021**, *6*, 26–32. [[CrossRef](#)]
31. Darmanin, T.; Guittard, F. Superoleophobic surfaces with short fluorinated chains? *Soft Matter* **2013**, *9*, 5982–5990. [[CrossRef](#)]
32. Prevedouros, K.; Cousins, I.T.; Buck, R.C.; Korzeniowski, S.H. Sources, fate and transport of perfluorocarboxylates. *Environ. Sci. Technol.* **2006**, *40*, 32–44. [[CrossRef](#)] [[PubMed](#)]
33. Berendjchi, A.; Khajavi, R.; Yazdanshenas, M.E. Fabrication of superhydrophobic and antibacterial surface on cotton fabric by doped silica-based sols with nanoparticles of copper. *Nanoscale Res. Lett.* **2011**, *6*, 594. [[CrossRef](#)] [[PubMed](#)]
34. Xu, L.; Wang, L.; Shen, Y.; Ding, Y.; Cai, Z. Preparation of hexadecyltrimethoxysilane-modified silica nanocomposite hydrosol and superhydrophobic cotton coating. *Fibers Polym.* **2015**, *16*, 1082–1091. [[CrossRef](#)]
35. Chang, H.; Tu, K.; Wang, X.; Liu, J. Facile preparation of stable superhydrophobic coatings on wood surfaces using silica-polymer nanocomposites. *BioResources* **2015**, *10*, 2585–2596. [[CrossRef](#)]
36. Chang, H.; Tu, K.; Wang, X.; Liu, J. Fabrication of mechanically durable superhydrophobic wood surfaces using polydimethylsiloxane and silica nanoparticles. *RSC Adv.* **2015**, *5*, 30647–30653. [[CrossRef](#)]
37. Manatunga, D.C.; de Silva, R.M.; de Silva, K.N. Double layer approach to create durable superhydrophobicity on cotton fabric using nano silica and auxiliary non fluorinated materials. *Appl. Surf. Sci.* **2016**, *360*, 777–788. [[CrossRef](#)]

38. Xu, B.; Zhang, Q. Preparation and Properties of Hydrophobically Modified Nano-SiO₂ with Hexadecyltrimethoxysilane. *ACS Omega* **2021**, *6*, 9764–9770. [[CrossRef](#)]
39. Vidal, K.; Gómez, E.; Goitandia, A.M.; Angulo-Ibáñez, A.; Aranzabe, E. The synthesis of a superhydrophobic and thermal stable silica coating via sol-gel process. *Coatings* **2019**, *9*, 627. [[CrossRef](#)]
40. Das, S.K.; Choi, S.U.; Yu, W.; Pradeep, T. *Nanofluids: Science and Technology*; John Wiley & Sons: Hoboken, NJ, USA, 2007.
41. Butler, T.; MacCraith, B.; McDonagh, C. Leaching in sol-gel-derived silica films for optical pH sensing. *J. Non-Cryst. Solids* **1998**, *224*, 249–258. [[CrossRef](#)]
42. Kim, G.H.; Hwang, S.W.; Kang, D.H.; Jung, B.N.; Lee, M.J.; Shim, J.K.; Seo, K.H. Controllable synthesis of silica nanoparticle size and packing efficiency onto PVP-functionalized PMMA via a sol-gel method. *J. Polym. Sci.* **2020**, *58*, 662–672. [[CrossRef](#)]
43. Li, Y.; Zhu, H.; Wang, Y.; Ray, U.; Zhu, S.; Dai, J.; Chen, C.; Fu, K.; Jang, S.H.; Henderson, D. Cellulose-Nanofiber-Enabled 3D Printing of a Carbon-Nanotube Microfiber Network. *Small Methods* **2017**, *1*, 1700222. [[CrossRef](#)]
44. Zhang, X.-F.; Feng, Y.; Huang, C.; Pan, Y.; Yao, J. Temperature-induced formation of cellulose nanofiber film with remarkably high gas separation performance. *Cellulose* **2017**, *24*, 5649–5656. [[CrossRef](#)]
45. Gopal, N.; Narasimhulu, K.; Rao, J. EPR, optical, infrared and Raman spectral studies of Actinolite mineral. *Spectrochim. Acta Part A Mol. Biomol. Spectrosc.* **2004**, *60*, 2441–2448. [[CrossRef](#)] [[PubMed](#)]
46. Al-Oweini, R.; El-Rassy, H. Synthesis and characterization by FTIR spectroscopy of silica aerogels prepared using several Si (OR)₄ and R'' Si (OR')₃ precursors. *J. Mol. Struct.* **2009**, *919*, 140–145. [[CrossRef](#)]
47. Ma, W.-S.; Li, J.; Deng, B.-J.; Zhao, X.-S. Preparation and characterization of long-chain alkyl silane-functionalized graphene film. *J. Mater. Sci.* **2013**, *48*, 156–161. [[CrossRef](#)]
48. Ray, S.; Maiti, C.; Lahiri, S.; Chakrabarti, N. Properties of silicon dioxide films deposited at low temperatures by microwave plasma enhanced decomposition of tetraethylorthosilicate. *J. Vac. Sci. Technol. B Microelectron. Nanometer Struct. Process. Meas. Phenom.* **1992**, *10*, 1139–1150. [[CrossRef](#)]
49. Pan, P.; Nesbit, L.; Douse, R.; Gleason, R. The composition and properties of PECVD silicon oxide films. *J. Electrochem. Soc.* **1985**, *132*, 2012. [[CrossRef](#)]
50. Wang, T.-H.; Gole, J.L.; White, M.G.; Watkins, C.; Street, S.C.; Fang, Z.; Dixon, D.A. The surprising oxidation state of fumed silica and the nature of water binding to silicon oxides and hydroxides. *Chem. Phys. Lett.* **2011**, *501*, 159–165. [[CrossRef](#)]
51. Zhong, Y.; Qiu, X.; Gao, J.; Guo, Z. Chemical structure of Si–O in silica fume from ferrosilicon production and its reactivity in alkali dissolution. *ISIJ Int.* **2019**, *59*, 1098–1104. [[CrossRef](#)]
52. Zeng, H.Z.; Zhang, W.X.; Zhang, W.L. XPS studies of charging effect induced by X-ray irradiation on amorphous SiO₂ thin films. *IOP Conf. Ser. Mater. Sci. Eng.* **2019**, *490*, 022079.
53. Orrabalis, C.; Rodríguez, D.; Pampillo, L.G.; Londoño-Calderón, C.; Trinidad, M.; Martínez-García, R. Characterization of Nanocellulose Obtained from *Cereus Forbesii* (a South American cactus). *Mater. Res.* **2019**, *22*, e20190243. [[CrossRef](#)]
54. Fisher, T.; Hajaligol, M.; Waymack, B.; Kellogg, D. Pyrolysis behavior and kinetics of biomass derived materials. *J. Anal. Appl. Pyrolysis* **2002**, *62*, 331–349. [[CrossRef](#)]
55. Burhenne, L.; Messmer, J.; Aicher, T.; Laborie, M.-P. The effect of the biomass components lignin, cellulose and hemicellulose on TGA and fixed bed pyrolysis. *J. Anal. Appl. Pyrolysis* **2013**, *101*, 177–184. [[CrossRef](#)]
56. Ray, S.S.; Okamoto, M. Polymer/layered silicate nanocomposites: A review from preparation to processing. *Prog. Polym. Sci.* **2003**, *28*, 1539–1641.
57. Zou, H.; Wu, S.; Shen, J. Polymer/silica nanocomposites: Preparation, characterization, properties, and applications. *Chem. Rev.* **2008**, *108*, 3893–3957. [[CrossRef](#)]
58. Camino, G.; Sgobbi, R.; Zaopo, A.; Colombier, S.; Scelza, C. Investigation of flame retardancy in EVA. *Fire Mater.* **2000**, *24*, 85–90. [[CrossRef](#)]
59. Böhm, L.; Cherdron, H.; Fleißner, M.; Kreuder, W.; Schneller, A. *Comprehensive Polymer Science: The Synthesis, Characterization, Reactions and Applications of Polymers*. (7 Bde.). Herausgegeben von G. Allen und J.C. Bevington. Pergamon Press, Oxford 1989. 5367 S., geb. \$1995.00.–ISBN 0-08-032516-5. *Angew. Chem.* **1990**, *102*, 345. [[CrossRef](#)]
60. Perera, H.J.; Latifi, R.; Blum, F.D. Development of structure in hexadecyltrimethoxysilane adsorbed on silica. *J. Phys. Chem. C* **2019**, *123*, 19005–19012. [[CrossRef](#)]
61. Ni, L.; Rigolet, S.; Chemtob, A.; Croutxé-Barghorn, C.; Brendlé, J.; Vidal, L. Head-to-head and head-to-tail multilayer n-alkylsilsesquioxane films. *Comptes Rendus Chim.* **2013**, *16*, 897–905. [[CrossRef](#)]
62. Dhôtel, A.; Li, H.; Fernandez-Ballester, L.; Delbreilh, L.; Youssef, B.; Zeng, X.C.; Tan, L. Supramolecular nanolayer reconfiguration after molecular intercalation. *J. Phys. Chem. C* **2011**, *115*, 10351–10356. [[CrossRef](#)]
63. Keene, M.T.; Gougeon, R.D.; Denoyel, R.; Harris, R.K.; Rouquerol, J.; Llewellyn, P.L. Calcination of the MCM-41 mesophase: Mechanism of surfactant thermal degradation and evolution of the porosity. *J. Mater. Chem.* **1999**, *9*, 2843–2849. [[CrossRef](#)]
64. Spataru, C.I.; Purcar, V.; Ghiurea, M.; Radovici, C.; Stanga, G.; Donescu, D. Effects of the nanoassociation of hexadecyltrimethoxysilane precursors on the sol-gel process. *J. Sol-Gel Sci. Technol.* **2013**, *65*, 344–352. [[CrossRef](#)]
65. Guo, M.; Yang, G.; Zhang, S.; Zhang, Y.; Gao, C.; Zhang, C.; Zhang, P. Co-modification of Bentonite by CTAB and Silane and its Performance in Oil-Based Drilling Mud. *Clays Clay Miner.* **2020**, *68*, 646–655. [[CrossRef](#)]
66. Chaikew, C.; Srikulkit, K. In situ synthesis of ABS containing hydrophobic silica nanoparticles and their effects on mechanical properties. *J. Sol-Gel Sci. Technol.* **2017**, *81*, 774–781. [[CrossRef](#)]